# Modeling of Carbon Dioxide Dissolution in an Injection Well for Geologic Sequestration in Aquifers

Federico Cao,[†] Dmitry Eskin,[‡,¶] and Yuri Leonenko[∗,§,‖]

†*Department of Mathematics, University of Toronto, Toronto, Ontario, Canada*

‡*Skolkovo Institute of Science & Technology, Moscow, Russia*

¶*The University of the West Indies, St. Augustine, Trinidad and Tobago (current address)*

§*Department of Earth and Environmental Sciences, University of Waterloo, Waterloo, Ontario, Canada*

‖*Department of Geography and Environmental Management, University of Waterloo, Waterloo, Ontario, Canada*

E-mail: leonenko@uwaterloo.ca

## Abstract

Carbon dioxide ($CO_2$) sequestration is considered to be one of the most effective technologies of mitigating greenhouse gas emissions. In this technology, single phase supercritical $CO_2$ is injected into an underground geological formation such as a deep saline aquifer. Existing sequestration projects demonstrate that successful implementations are possible; however, significant uncertainties associated with the risks of leakage remain an obstacle for broader use of this technology. The security of underground disposal could be considerably increased by dissolving the $CO_2$ in a brine produced

from the aquifer, then re-injecting the mixture underground. The dissolution process occurs before the mixture reaches the aquifer; this significantly reduces or completely eliminates the risks of $CO_2$ leakage. This technique can drastically extend the amount of worldwide aquifers available for carbon sequestration. As was previously shown, complete dissolution could be achieved in a surface pipeline operating under the pressure of a target aquifer, where $CO_2$ is injected. In this paper, a comprehensive model of $CO_2$ droplet dissolution in a vertical injection well is presented. The model accounts for droplet breakup, coalescence, and dissolution processes as well as temperature and pressure variations over well depth. Feasibility and results are discussed and compared with surface dissolution options.

# Keywords

Carbon dioxide, geologic storage, droplets dissolution, modeling, pipe flow, enhancing security of carbon sequestration

# 1    Introduction

Since the onset of the Industrial Revolution, the use of fossil fuels has exploded exponentially around the world. Due to its abundance and cheap availability in comparison to "clean" renewable alternatives, it is likely to remain the world's primary energy source for decades ahead. As a result, to match the ever-growing demand for energy, both the production and consumption of fossil fuels have continued to accelerate (IEA, 2019). Due to this demand, annual global carbon emissions from fossil fuels have reached nearly 10 billion metric tons in 2014 (Boden et al., 2017) and continue to climb. As carbon dioxide and other greenhouse gas levels rise, contributing to anthropogenic global warming, the repercussions are numerous. From greater vector transmissions to increased flooding due to rising ocean levels, it is clear that combating anthropogenic global warming is of significant importance. A key step

towards this goal is the reduction of $CO_2$ and other greenhouse gases in the atmosphere. The Intergovernmental Panel of Climate Change (IPCC) has reported that carbon capture and storage (CCS) technology is a promising solution for significantly lowering the amount of $CO_2$ in the atmosphere (Metz et al., 2005).

There exist many technologies; however, there is substantial interest in geological sequestration in sedimentary formations. This form of sequestration involves storage in depleted oil and gas reservoirs (Herzog, 2001; Jenkins et al., 2012), unmineable coal bed reservoirs (Shi and Durucan, 2005), or deep saline aquifers (Celia et al., 2015). Another possible option is ocean sequestration, where $CO_2$ is injected into the ocean (Haugan and Joos, 2004). Though, ocean sequestration has its own drawbacks, such as ocean acidification.

Overall, deep saline aquifers have the greatest long term potential for carbon sequestration (International Energy Agency (IEA), 2008); in fact, it has been estimated that the storage capacity of deep saline aquifers is around 2000 Gigatons (Gt) of $CO_2$ (Metz et al., 2005). This is approximately two orders of magnitude greater than the total annual worldwide emissions, making deep saline aquifers a viable option of $CO_2$ storage.

There are, however, considerable uncertainties regarding storage security. General overview and challenges of sequestration in sedimentary formations can be found in Benson and Cole (2008). Further, many particular challenges and new fates could be discovered while studying the feasibility and characterization of potential formation for commercial implementation of CCS (Ghaderi and Leonenko, 2009; Ghaderi and Leonenko, 2015).

In our opinion, the main technical challenge that CCS faces is the risk of leakage. Since injected $CO_2$ is less dense than that of resident brine, $CO_2$ may leak and flow upwards through high permeability zones such as natural fractures or abandoned wells. Furthermore, cap-rocks that have confined buoyant oil and gas have not been proven to confine buoyant $CO_2$ for the same geologic time scales (van der Meer, 1993; Lindeberg, 1997). After injection into the aquifer, the $CO_2$ starts to dissolve by diffusion or natural convection. The latter

process is strongly dependent on reservoir parameters. This phenomenon is studied in the work of Emami-Meybodi et al. (2015) where it was found that the time scale for complete dissolution could reach $10^3 - 10^5$ years. Thus, a safe approach that minimizes the risks of storage security is greatly needed for implementing CCS technologies. One of the most promising ways to increase storage security is to accelerate the dissolution of $CO_2$ in a formation brine.

To speed up dissolution, many engineering options have been previously suggested. Hassanzadeh et al. (2009) and Keith et al. (2005) proposed a method for enhancing in-situ $CO_2$ dissolution by injecting brine on top of the injected $CO_2$. Subsequently, Leonenko and Keith (2008) introduced a method of dissolving $CO_2$ before it is injected underground. This method could be achieved within a surface (ex-situ) pipeline where a two phase $CO_2$-brine droplet regime flow takes place. The generation and dissolution of $CO_2$ droplets occur in a turbulent pipe flow. Placing additional equipment such as a static mixer (Zirrahi et al., 2013a), a downhole mixer (Zirrahi et al., 2013b) or specially designing an injection well where brine and $CO_2$ are co-injected (Shafaei et al., 2012) can further improve dissolution rates.

Different aspects of technical and economic feasibility of surface ex-situ dissolution have been built up and developed by authors in the following studies: Turbulent (Zendehboudi et al., 2011) and laminar (Cholewinski and Leonenko, 2013) regimes of mass transfer from $CO_2$ droplets into brine during co-current pipeline flow were studied and summarized in Leonenko (2018).

The above studies, however, did not include droplet breakup and coalescence. Recently, a comprehensive modeling of ex-situ dissolution involving the major phenomena, which occur in a pipeline (droplet coalescence, breakup, and dissolution), was performed and validated using available experimental data (Cao et al., 2020).

In the present study, we present a detailed model of $CO_2$ dissolution in an injection well,

which could potentially be more economical. The following schematic (Fig. 1) describes how this process may be achieved: Brine is extracted from the production site, mixed with $CO_2$, and then injected into the well. The $CO_2$ dissolves as the mixture flows through the tubing towards the aquifer. Although the model developed is based on the prior studies of Cao
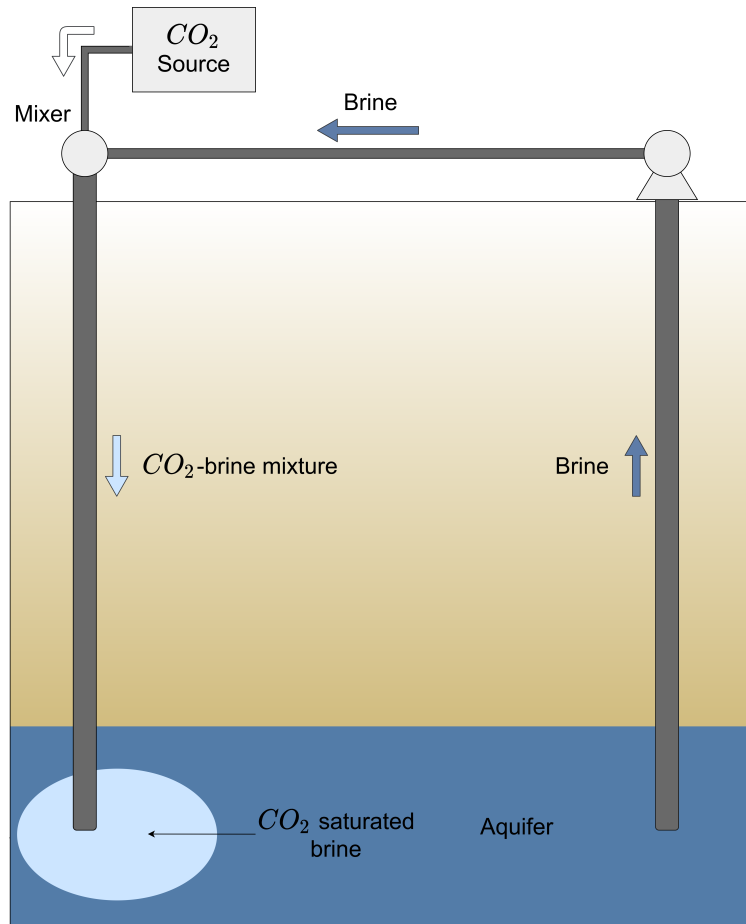


Figure 1: Schematic of $CO_2$ dissolution in an injection well. The $CO_2$ is mixed with brine extracted from the production site at the surface, then the mixture is injected into the vertical well. $CO_2$ dissolution occurs as the mixture flows through the tubing due to turbulent flow.

et al. (2020), it accounts for the effects of both the pressure and temperature distributions along the vertical well on droplet solubility. The computational results are compared with those calculated for horizontal surface pipelines. The system conditions corresponding to completely dissolving $CO_2$ droplets in an injection well ahead of reaching a target aquifer is demonstrated.

# 2 Model

To a great extent, the model presented in this study is based on the former study conducted by Cao et al. (2020). In contrast to the previous work, the present model accounts for the effects of both a hydrostatics-induced pressure increase in a vertical well and a temperature increase with well depth due to the geothermal gradient on the solubility of $CO_2$ droplets.

Further, we formulate the model in full detail.

## 2.1 Governing model equation

The major modeling assumptions are as follows:

1. Flow is steady-state.

2. Flow is axisymmetric.

3. Pipe is either vertical or horizontal. If the pipe is horizontal, droplet stratification caused by gravity is ignored.

4. A continuous droplet size distribution is substituted with a discrete distribution composed of a finite number of size fractions.

The advection-diffusion population balance equation for steady-state flow in cylindrical coordinates for a dispersed phase with $M$ size fractions can be formulated as (Eskin et al., 2017a)

$$[u(r) - u_{B_i}(r)]\frac{\partial N_i}{\partial x} = \frac{1}{r}\frac{\partial}{\partial r}\left(rD_i(r)\frac{\partial N_i}{\partial r}\right) + [u(r) - u_{B_i}(r)]\left(\frac{\partial N_i}{\partial x}\right)_{PB}, \quad i = 1, ..., M, \quad (1)$$

where $i$ is the size fraction number, $r$ is the radial coordinate, $x$ is the coordinate along the pipe axis, $u(r)$ is the flow velocity, $u_{B_i}(r)$ is the droplet rising velocity of the $i$-th size fraction, $N_i$ is the number concentration of droplets of the $i$-th size fraction in a computational cell,

$D_i(r)$ is the turbulent diffusivity of a droplet of the $i$-th size fraction, and $\left(\dfrac{\partial N_i}{\partial x}\right)_{PB}$ is the number concentration derivative accounting for coalescence, breakup and dissolution for the $i$-th size fraction. The boundary conditions for Eq. (1) are

1. The flux through the pipe wall is zero:

$$q_i(R) = -D_i\frac{\partial N_i}{\partial r}\bigg|_{r=R} = 0. \tag{2}$$

2. The dispersed phase concentration gradient at the pipe center is zero:

$$\frac{\partial N_i}{\partial r}\bigg|_{r=0} = 0. \tag{3}$$

3. The initial droplet size distribution $\Psi_i(r)$ is known (input parameter):

$$N_i(0, r) = \Psi_i(r). \tag{4}$$

Eq. (1) can be formulated in a one-dimensional time-dependent coordinate system moving with mean flow velocity $U$ as follows:

$$\frac{u(r) - u_{B_i}(r)}{U}\frac{\partial N_i}{\partial t} = \frac{1}{r}\frac{\partial}{\partial r}r\left(D_i(r)\frac{\partial N_i}{\partial r}\right) + \frac{u(r) - u_{B_i}(r)}{U}\left(\frac{\partial N_i}{\partial t}\right)_{PB} \tag{5}$$

where $dt = dx/U$.

Solving Eq. (5) is more convenient than solving Eq. (1) because the population balance model equations are formulated in a time-dependent form. To solve Eq. (5), a number of parameters and functions of Eq. (5) should be determined.

## 2.2 Key sub-models required for the solution of the advection-diffusion population balance equation

### 2.2.1 Flow velocity distribution across a pipe

The steady-state velocity distribution $u(r)$ along a pipe radius is described by the simple Prandtl-Karman model (Schlichting and Gersten, 2000). The flow field consists of two regions. The first is a viscous boundary layer in the wall vicinity, characterized by a linear velocity distribution. The second region, outside of the viscous layer, is a turbulent core flow, characterized by a logarithmic velocity distribution. In dimensionless coordinates, the velocity distribution along a pipe radius is formulated as (Schlichting and Gersten, 2000)

$$u^+ = y^+, \quad y^+ \leq 11.6 \tag{6}$$

$$u^+ = 2.5 \ln y^+ + 5.5, \quad y^+ > 11.6 \tag{7}$$

where $u^+ = u/u_*$ is the dimensionless flow velocity, $u_* = (\tau_w/\rho_f)^{0.5}$ is the frictional velocity, $y^+ = u_* y/\nu_f$ is the dimensionless coordinate, $y = R - r$ is the distance from the wall, $\nu_f$ is the fluid kinematic viscosity, and $\tau_w$ is the wall shear stress.

### 2.2.2 Turbulent diffusivity of droplets

The droplet turbulent diffusivity is expressed as

$$D_p = \frac{D_t}{Sc_{pt}} \tag{8}$$

where $D_t = v_t/Sc_t$ is the turbulent diffusivity, $v_t$ is the eddy diffusivity, $Sc_t$ is the Schmidt number for turbulent flow, and $Sc_{pt}$ is the droplet Schmidt number.

Given that the droplet sizes and differences between the densities of the fluid and dispersed phase are small, we assume that the droplet turbulent diffusivity is equal to the eddy diffu-

sivity,

$$D_i = v_t. \tag{9}$$

The dimensionless eddy diffusivity distribution over a pipe radius can be calculated with the empirical equations (Johansen, 1991)

$$v_t^+ \approx \frac{v_t}{\nu_f} = \left(\frac{y^+}{11.15}\right)^3 \quad \text{for} \quad y^+ \leq 3 \tag{10}$$

$$v_t^+ \approx \left(\frac{y^+}{11.4}\right)^2 - 0.049774 \quad \text{for} \quad 3 < y^+ \leq 52.108 \tag{11}$$

$$v_t^+ \approx \kappa y^+ \quad \text{for} \quad y^+ > 52.108 \tag{12}$$

where $\kappa = 0.406$ is the von-Karman constant.

## 2.3 Coalescence, breakup, and dissolution modeling

The total number concentration derivative is expressed as the sum of the number concentration derivatives involving breakup, coalescence, and dissolution,

$$\left(\frac{\partial N_i}{\partial t}\right)_{PB} = \left(\frac{\partial N_i}{\partial t}\right)_{break} + \left(\frac{\partial N_i}{\partial t}\right)_{coal} + \left(\frac{\partial N_i}{\partial t}\right)_{diss}. \tag{13}$$

The terms composing Eq. (13) are described in detail in the Appendix.

## 2.4 Other sub-models needed for dispersion simulations

Both the pressure and temperature of the $CO_2$-brine mixture change along a vertical well. The solubility of $CO_2$ in brine is a function of both the pressure and temperature. The employed procedure of solubility calculation is given in the Appendix. The pressure increase with well depth is determined by hydrostatics, whereas the temperature change is determined by the geothermal gradient and the heat exchange between the mixture flowing in the tubing

and the surrounding formation.

### 2.4.1 Heat transfer between formation and mixture flow in a pipe

The temperature distribution along the well depth is determined by heat transfer between the fluid flowing in the tubing and the surrounding formation. In this work, we account for the variation of the formation temperature as a result of the geothermal gradient. In typical continental crusts, the geothermal gradient is approximately 25 °C/km within the first $3 - 5$ km of the Earth's surface (DiPietro, 2013). Thus, it is reasonable to assume that the formation temperature increases linearly along a well depth that does not exceed $3 - 5$ km. Then, the formation temperature $T_{form}$ is calculated as $T_{form}(z) = T_0 + T_{grad}z$, where $T_0$ is the initial formation temperature at the surface.

In the present work, we assume a simplified well structure: a steel pipe, surrounded by a cement layer, is embedded into a porous formation (Fig. 2).

The heat flux through the inner tubing wall is calculated as

$$q = \frac{1}{1/v_1 + R/(r_{cem}v_2)}(T - T_{form}), \tag{14}$$

where $r_{cem}$ is the outer radius of the cement layer, $T$ is the mean fluid temperature in the pipe, $T_{form}$ is the formation temperature, $v_1$ is the heat transfer coefficient from the fluid in a pipe to the formation boundary, and $v_2$ is the heat transfer coefficient accounting for the non-steady-state heat conduction through the formation. These heat transfer coefficients are calculated as (Bahonar et al., 2011),

$$\frac{1}{v_1} = R\left(\frac{1}{\alpha R} + \frac{1}{\lambda_{wall}}\ln\left(1 + \frac{\delta_{wall}}{R}\right) + \frac{1}{\lambda_{cem}}\ln\left(\frac{r_{cem}}{R + \delta_{wall}}\right)\right) \tag{15}$$

$$\frac{1}{v_2} = \frac{r_{cem}f(t_{inj})}{\lambda_{form}}, \tag{16}$$

where $\alpha$ is the heat conduction coefficient from a fluid flow to the tubing wall, $\delta_{wall}$ is the

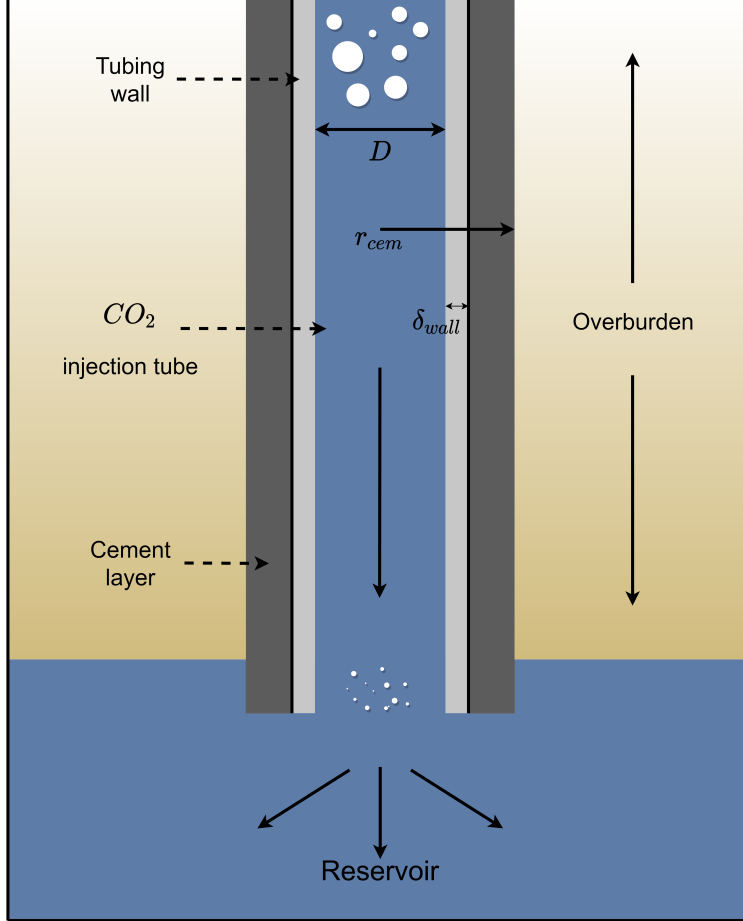Figure 2: Cross section of the well structure for $CO_2$ injection. It consists of a steel pipe with thickness $\delta_{wall}$ surrounded by a cement layer of radius $r_{cem}$. The droplets dissolve due to turbulent flow and are injected into the reservoir.

thickness of the pipe wall, $\lambda_{form}$ is the formation thermal conductivity, and $f(t_{inj})$ is the semi-empirical dimensionless function of injection time accounting for non-steady state heat conduction through porous rock.

The heat transfer coefficient $\alpha$ is defined as

$$\alpha = \frac{\lambda_w Nu}{D}, \tag{17}$$

where $Nu$ is the Nusselt number and $\lambda_w$ is the thermal conductivity of a fluid (water) in a pipe.

To calculate the Nusselt number, we used the following correlation for convective heat transfer in a turbulent tubing flow (e.g. Incropera and DeWitt, 1996):

$$Nu = 0.023 Re^{0.8} Pr^{0.4}, \tag{18}$$

where $Pr = \dfrac{\nu}{\lambda_w / \rho_f c_f}$ is the Prandtl number.

The thermal conductivity of water has been calculated using the correlation of Coker (1995),

$$\lambda_w = A + BT + CT^2, \tag{19}$$

where $A = -0.2758$, $B = 4.6120 \times 10^{-3}$, $C = -5.5391 \times 10^{-6}$ are correlation constants.

Different correlations for the dimensionless heat-conduction time function $f(t_{inj})$ were obtained by several authors as asymptotic solutions of the one-dimensional non-steady-state heat conduction equation for a porous rock (Fontanilla and Aziz, 1982; Ramey, 1962; Hasan and Kabir, 1994). Bahonar et al. (2011) showed that the correlation of Hasan and Kabir (1994) is characterized by a rather high accuracy for a wide range of injection times and therefore, can be confidently used in engineering applications. This correlation is written in the following form (Hasan and Kabir, 1994):

$$f(t_{inj}) = \ln(e^{-0.2t_D} + (1.5 - 0.3719e^{-t_D})\sqrt{t_D}), \tag{20}$$

where $t_D = \dfrac{a_{form} t_{inj}}{r_{cem}^2}$ is the dimensionless brine injection time and $a_{form}$ is the formation thermal diffusivity.

The temperature variation along a tubing is calculated from the enthalpy definition as

$$\frac{dT}{dz} = \left( \frac{di_m}{dz} - \frac{1}{\rho_m} \frac{dp}{dz} \right) \frac{1}{c_{pm}}, \tag{21}$$

where $i_m$ is the mixture enthalpy, $c_{pm}$ is the mixture heat capacity, $\rho_m$ is the mixture density,

$\dfrac{dp}{dz} = \rho g + \dfrac{dp}{dz}_{fr}$ is the total pressure gradient, and $\dfrac{dp}{dz}_{fr}$ is the friction pressure gradient.

The enthalpy of the mixture flowing through the tubing is calculated by the following equation, obtained from the energy balance for a liquid flowing in a vertical pipe, as

$$\frac{di_m}{dz} = -\frac{q\pi D}{\dot{M}} + g, \tag{22}$$

where $\dot{M}$ denotes the mixture mass flow rate.

# 3    Numerical examples and discussion

For the numerical solution of the advection-diffusion population balance equation, describing the complex process of droplet dissolution in a vertical turbulent pipe flow, a MATLAB code was developed.

Nearly all the equations used in the code have been presented in Section 2 as well as in the Appendix. The only detail that has not yet been clarified is the droplet-fluid relative velocity. This has been calculated from the steady-state balance of the buoyancy and drag forces acting on a droplet. Considering that in a real mixture a droplet surface is nearly rigid due to unavoidable contamination (Levich, 1962), the drag force coefficient was calculated by a correlation for a spherical particle in a turbulent flow.

For the numerical analysis of the dissolution of liquid $CO_2$ droplets, a number of computations were conducted for a pipe of 1000 m length and 0.15 m diameter. The following injection system parameters were selected. The surface temperature and pressure were set to $T = 25$ °C and $p = 70$ bar respectively. The droplet density was set to 743 kg/m$^3$, while the fluid density was set to 997 kg/m$^3$. The brine viscosity was calculated using an empirical correlation for water (Likhachev, 2003), valid for a wide range of temperatures (273-464 K) and pressures (1-250 bar). The interfacial tension (IFT), required for calcula-

tion of the droplet Weber number, was assumed to be 0.025 N/m. Although IFT depends on the pressure, temperature and water salinity, the selected value is a good average estimate for a $CO_2$-water system in the range of temperatures and pressures considered in our work (Bachu and Bennion, 2009; Nielsen et al., 2012). Note that relatively small variations of the interfacial tension, which may occur in real turbulent mixture flows, do not lead to significant changes in droplet sizes (Eskin et al., 2017a).

Also, for the chosen temperature and pressure conditions, which are slightly below the critical temperature and pressure for supercritical $CO_2$ ($T_{crit} = 31$ °C, $p_{crit} = 73.8$ bar), the droplets are in a liquid state. In the calculations conducted, the injection time was chosen to be 2 days. It is worth emphasizing that an increase in the fluid temperature, caused by heat exchange with the rock whose temperature increases with depth due to the geothermal gradient, is small. This smallness is explained by the following two reasons: 1) relatively short fluid residence time in the tubing; 2) rather low heat flux from the rock to the flowing fluid. Therefore, a fluid temperature increase along the entire simulated depth (1 km) does not exceed 1 °C, whereas a pressure increase, caused mainly by the hydrostatic effect, exceeds 150 bar. Thus, at the bottom of the wellbore, the pressure is significantly higher than the critical value, whereas the temperature is not; therefore, the $CO_2$ remains in a liquid state. Note that for greater depths, the temperature can also exceed the critical value, resulting in a supercritical $CO_2$ state. The solubility calculations were conducted using the method suggested by Spycher et al. (2003). The calculation details are given in Section iv of the Appendix. Note that this method has also been successfully used by other investigators (e.g. Hassanzadeh et al., 2008). This approach provides accurate solubility results for temperatures in the range of $12 - 100$ °C and pressures up to 600 bar. Because this method is based on the Redlich-Kwong equation of state, which describes $CO_2$ behavior under both subcritical and supercritical conditions, the calculation accuracy weakly depends on small variations of $CO_2$ pressure and temperature in the critical point vicinity.

In Fig. 3, we showed both the temperature and pressure distributions along the wellbore depth. The calculations were conducted for a $CO_2$-water dispersion flowing downwards with mean flow velocity $U = 1.45$ m/s in a pipe with inner diameter $D = 0.15$ m. The geothermal gradient was assumed to be equal to 25 °C/km. In Fig. 3a, one can see the fluid temperature distributions calculated for the different injection times: 20 min, 2 days and 1 year. The fluid temperature variation along the pipe is negligibly small for all of the cases. The pressure distribution (Fig. 3b), determined by hydrostatics, is linear.
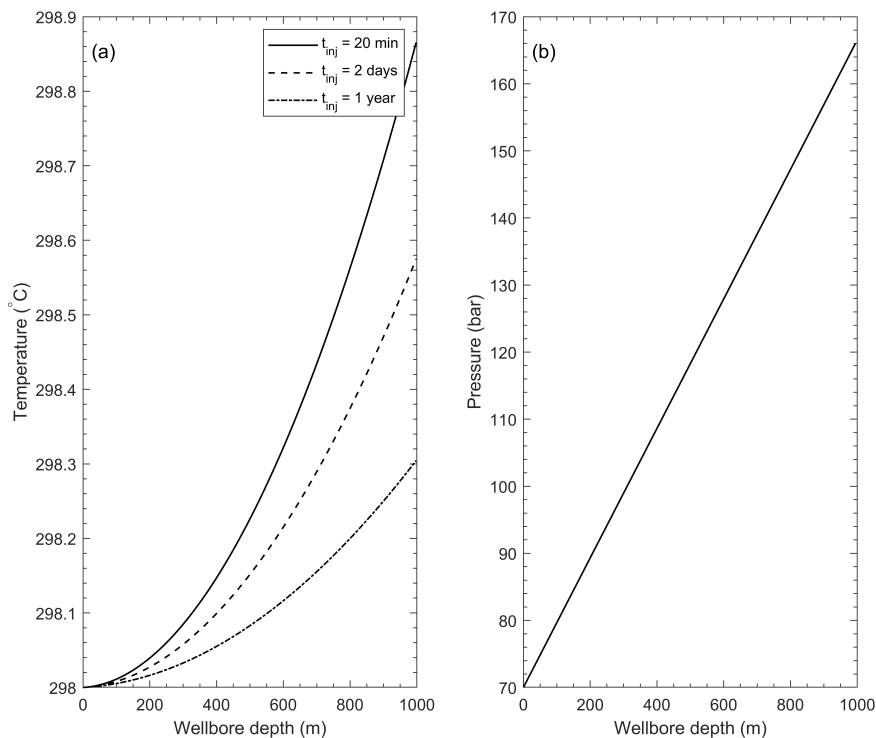


Figure 3: Temperature (a) and pressure (b) distributions along the wellbore depth.

A comprehensive list of parameters used for the modeling is given in Table. 1.

Note that for real injection systems, the amount of dissolved $CO_2$ should not exceed the maximum solubility at reservoir conditions in order to prevent the escape of $CO_2$ from the solution.

15

Table 1: Physical parameters

| Parameter | Value | Units |
|---|---|---|
| Pipe length | 1000 | m |
| Pipe diameter | 0.15 | m |
| Wall thickness | 0.0139 | m |
| Cement thickness | 0.0921 | m |
| Thermal conductivity (overburden) | 1.73 | W/m K |
| Thermal conductivity (steel) | 48 | W/m K |
| Thermal conductivity (cement) | 0.87 | W/m K |
| Heat capacity (overburden) | 2000 | J/kg K |
| Heat capacity (water) | 4181 | J/kg K |
| Heat capacity ($CO_2$) | 660 | J/kg K |
| Overburden density | 2700 | kg/m$^3$ |
| Fluid density | 997 | kg/m$^3$ |
| Droplet density | 743.1 | kg/m$^3$ |
| Surface pressure | 70 | bar |
| Initial fluid temperature | 298 | K |
| Initial geothermal temperature | 298 | K |
| Universal gas constant | 8.314 | J/mol K |
| Interfacial tension | 0.025 | N/m |

The pipe radius was discretized using 30 cells. The number of droplet size fractions was selected to be 40. The time step was set to $10^{-4}$ s.

Note that further, we compare the computational results obtained for a vertical pipeline flow with the results for a horizontal flow. The temperature distribution along a vertical tubing depends on the injection duration, as seen in Fig. 3. Typical $CO_2$ injection times are on the order of years. We would like to emphasize that due to an intense cooling of the formation layer, caused by heat exchange with the flowing mixture, the mixture temperature increase along the tubing is rapidly reduced.

Note also that the computations of horizontal flows were conducted assuming a uniform droplet distribution over a pipe cross-section; i.e., droplet stratification due to gravity was neglected. The rationale of this assumption for $CO_2$ droplet dispersion in turbulent pipe flows at high flow rates was discussed in the paper of Cao et al. (2020). The major reason is small droplet inertia in dispersion flows, characterized by small droplet sizes. Thus, the formal

difference between computations of vertical and horizontal dispersion flows is as follows: Droplet buoyancy, causing droplet – continuous fluid velocity difference, was introduced for a vertical flow. A change in the carbon dioxide solubility in water with well depth due to both an increase in pressure caused by hydrostatics and a mixture temperature increase caused by heat flux from formation was taken into account for a vertical flow (see Section iv). Note that the flow parameters were assumed to be the same as those used by Cao et al. (2020) in their work on dissolution modeling in horizontal pipe flows.

In Fig. 4, we present a comparison of distributions of the droplet holdups (volume concentrations) along the tubing for the same mean mixture flow velocity and the three different initial droplet holdups. The holdups decrease faster in the vertical pipe flows than in the horizontal ones due to the droplet solubility increase with well depth. An increase in the initial holdup leads to significantly larger droplet sizes due to a reduction in the dissolution rate with an increase in the droplet concentration.
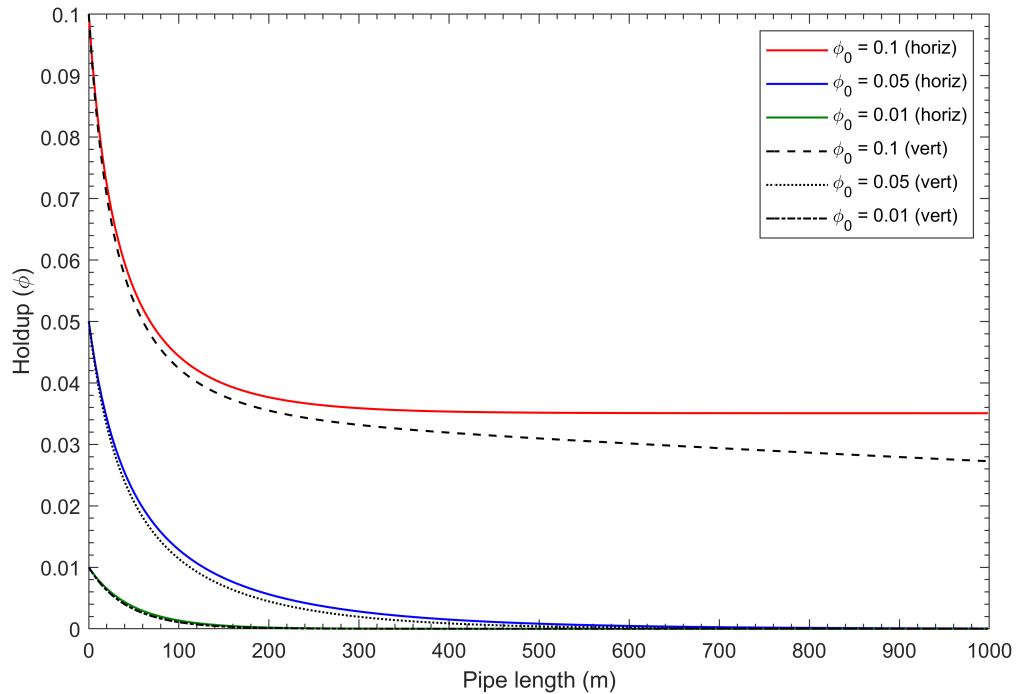


Figure 4: Droplet holdup evolution along horizontal and vertical pipes for different initial holdups at a constant mean flow velocity of $v = 3.63$ m/s.

In Fig. 5, one can see the droplet holdup decreases along horizontal and vertical pipelines for different mean flow velocities at a constant $CO_2$ flow rate. The differences between the distribution computed for the horizontal and vertical flows are small because the holdup values are rapidly reduced to zero for all of the cases considered. Therefore, the moderate solubility increase with well depth for the vertical flows weakly affects the holdup distribution curves.
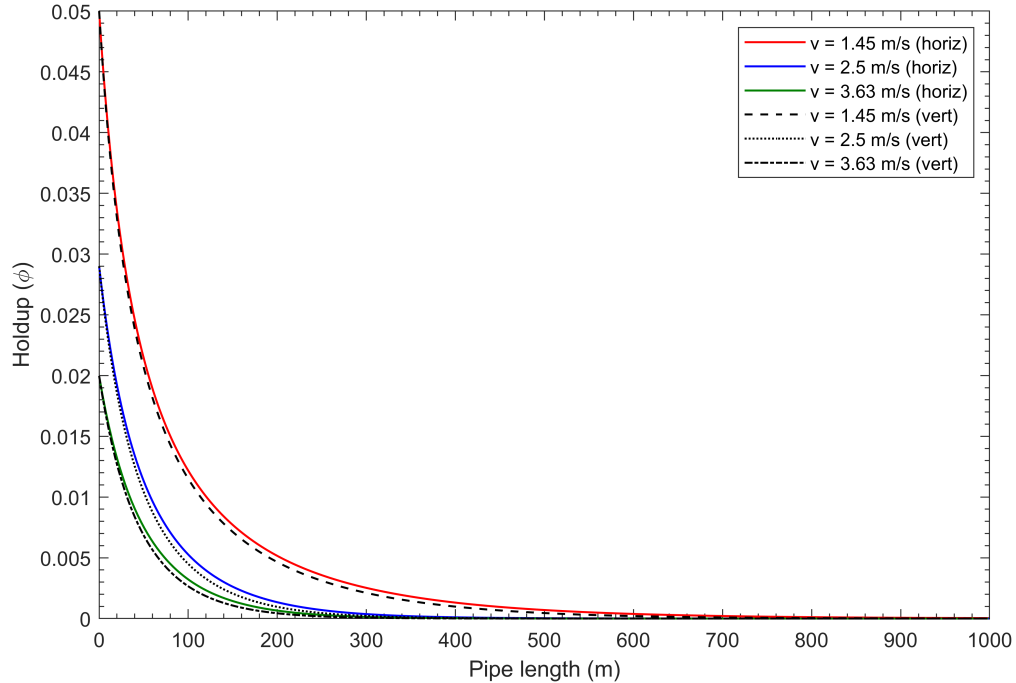


Figure 5: Droplet holdup evolution along horizontal and vertical pipes for different mixture flow velocities at the same $CO_2$ flow rate.

In Fig. 6, one can see the comparison of the droplet Sauter mean diameter distributions along the vertical pipeline, computed for the different mean flow velocities, with the corresponding diameter distributions obtained for the horizontal pipeline. The computations were performed assuming the initial droplet holdup to be $\phi_0 = 0.05$. One can see that the droplet Sauter mean diameter distributions along the vertical and horizontal pipes are similar. Nevertheless, the Sauter diameters in the vertical flows are larger at the initial (first) section of the pipeline, but become smaller, decreasing at a greater rate than in the horizontal flow for the second pipe section. This observation can be explained as follows. The

18

solubility of droplets in water decreases with a temperature increase and increases with a pressure increase. The solubility reduction due to a temperature increase is very small. A phenomenon, important for understanding the behavior of the curves in Fig. 6, is associated with droplet rising in a vertical pipe. According to Eq. 5, the multiplier $(u(r) - u_{B_i})/U$ becomes negative in the near-wall vicinity. After dividing all of the terms of Eq. 5 by this multiplier, it is possible to see that its sign change is equivalent to a sign change of the diffusion term in Eq. 5 to a negative value. This effect prevents turbulent diffusion-induced migration of large droplets towards the wall and small ones outward the wall in the near-wall area where the droplet breakup rate is the highest. Therefore, the predicted droplet Sauter dimeters along the first section of the vertical pipe are larger than those along the horizontal pipe. As one can see from Fig. 6 the described effect is stronger for a small mean flow velocity because the ratio of the droplet rising velocity to the mean flow velocity is higher in this case. Overall, this effect is rather small and the accuracy of its calculation is low because of the following reasons. First, the model of droplet dispersion, employed in our work, does not account for a rather significant wall effect on the droplet rising velocity. Second, the employed linear velocity profile in the wall vicinity is characterized by a moderate accuracy. However, the smallness of the effect, associated with droplet rising, makes it ignorable in engineering calculations.

Except this rather small effect, a solubility increase due to an increase in the hydrostatic pressure along a vertical pipe is a dominating factor, which leads to a reduction in the droplet sizes to values lower than those observed in the horizontal flow.

In Fig. 7, we present a comparison of the droplet Sauter mean diameter distributions along the horizontal and vertical pipes for a constant $CO_2$ flow rate. In this case, the initial droplet holdup is inversely proportional to the mean flow velocity. The highest holdup, $\phi_0 = 0.05$, corresponds to the lowest velocity, $v = 1.45$ m/s. One can see that the droplet size evolutions along the pipes are somewhat similar to those observed in Fig. 6. However,
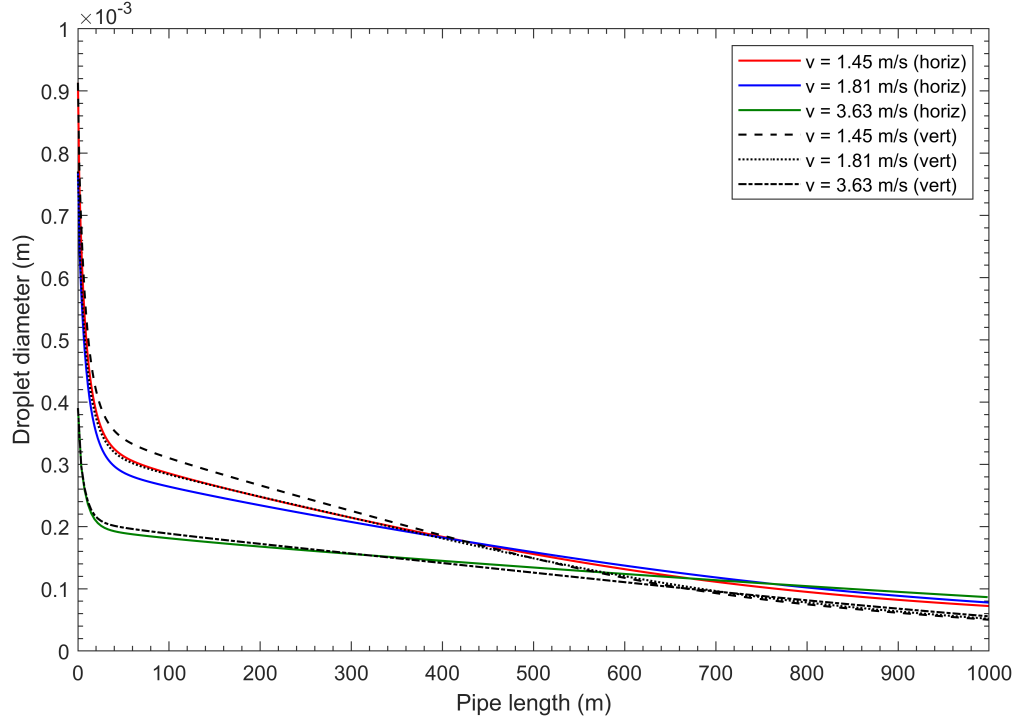
Figure 6: Comparison of droplet Sauter mean diameters along horizontal and vertical pipes for mean flow velocities at a constant initial $CO_2$ holdup.

since in the present case, the initial droplet concentration decreases with a flow velocity increase, the Sauter diameters decrease faster with an increase in the flow velocity than in the case of the fixed initial droplet holdup.

In Fig. 8, we illustrate an effect of the initial droplet volume fraction on the distributions of the droplet Sauter mean diameter along the vertical and horizontal pipelines for the same mean flow velocity. The higher the initial droplet holdup, the lower the droplet dissolution rate. An effect of the pipe orientation is significant only at relatively low holdups. At the highest droplet holdup considered, the dissolution rate is low; therefore, an enhanced droplet solubility in the vertical pipe slightly affects the droplet size reduction with well depth. The lower the droplet holdup, the stronger the solubility increase influences the droplet size reduction. However, if the initial droplet holdup is very low and a complete droplet dissolution occurs, then the final droplet size is zero, indicating complete droplet dissolution for both the vertical and horizontal pipes.
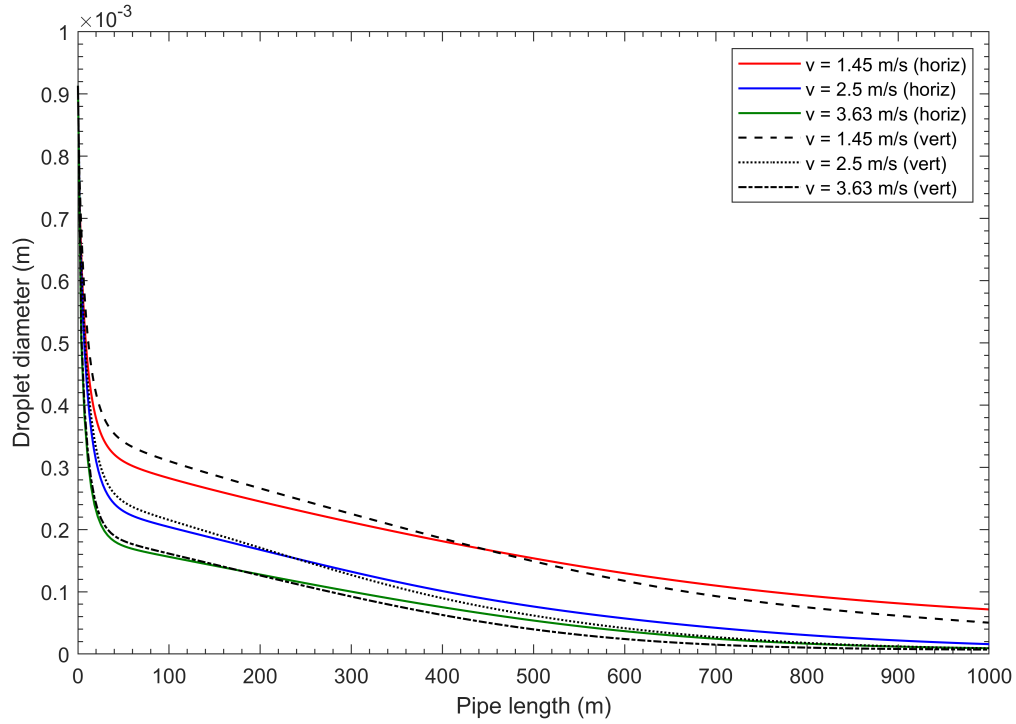
20

Figure 7: Comparison of droplet Sauter mean diameter evolution along horizontal and vertical pipes for mean flow velocities at a constant $CO_2$ flow rate.
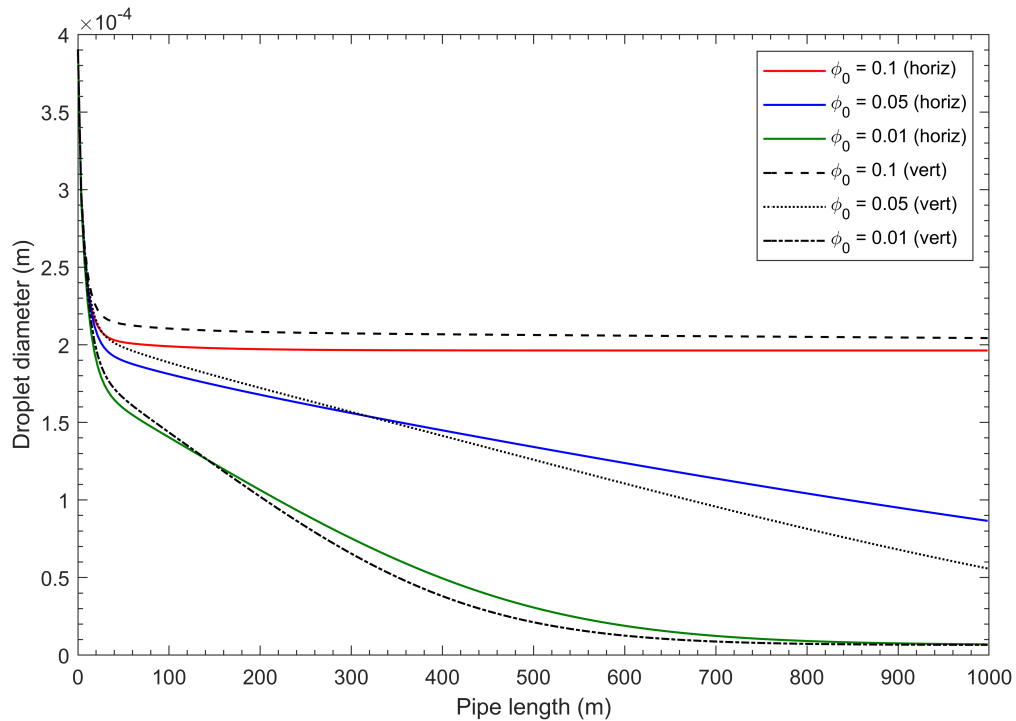


Figure 8: Comparison of droplet Sauter mean diameter evolution along horizontal and vertical pipes for different initial holdups at $v = 3.63$ m/s.

# 4    Conclusion

A comprehensive model of $CO_2$ droplet dissolution, accompanied by breakup and coalescence, has been developed for a vertical turbulent tubing flow. The model, reduced to an advection-diffusion population balance equation, describes droplet size evolution along an injection well. The fixed pivot method of Kumar and Ramkrishna (1996) was used for the numerical representation of the population balance related terms of the equation.

Effects of pressure and temperature, varying along the well, on $CO_2$ solubility in water were also taken into account.

The corresponding computational code was written in MATLAB. The advection-diffusion population balance equation was solved using the finite difference method. Distributions of droplet holdups and mean Sauter diameters computed in a vertical pipeline were compared with those in horizontal pipelines. The computations showed that the dissolution rate in a vertical pipe flow is higher than that in a horizontal flow due to an increase in $CO_2$ solubility with an increase in pressure. The pressure in a vertical pipe increases with well depth due to hydrostatics. However, it is important to emphasize that the dissolution enhancement in a vertical flow in comparison to a horizontal flow is relatively small and does not dramatically affect the dissolution process in a pipe.

Both horizontal and vertical tubings are technically feasible to completely dissolve dispersed phase $CO_2$ before it reaches the target aquifer, but the latter could be more economical because it allows the utilization of depleted hydrocarbon wells.

# Appendix

## A.I   Population balance

The population balance term requires a numerical representation of the population balance equation accounting for droplet breakup, coalescence, and dissolution. In the present work, we employed the fixed pivot method of Kumar and Ramkrishna (1996). In order to solve Eq. (13), the corresponding models of droplet breakup, coalescence, and dissolution should be chosen.

### i   Breakup term

To model droplet breakup, we assume that the fragmentation of a mother droplet leads to the formation of two daughter droplets. The rate of number concentration change due to breakup is numerically calculated as (Kumar and Ramkrishna, 1996)

$$\left(\frac{\partial N_i}{\partial t}\right)_{break} = \sum_{k=1}^{M} n_{i,k} G_k N_k - G_i N_i, \tag{A.1}$$

where $G_i$ is the specific breakup rate of a droplet belonging to the $i$-th size fraction. The function $n_{i,k}$ is calculated as (Kumar and Ramkrishna, 1996)

$$n_{i,k} = \int_{x_i}^{x_{i+1}} \frac{x_{i+1} - v}{x_{i+1} - x_i} \beta(v, x_k) dv + \int_{x_{i-1}}^{x_i} \frac{v - x_{i-1}}{x_i - x_{i-1}} \beta(v, x_k) dv, \tag{A.2}$$

where $\beta(v, x_k)$ is the droplet breakup density function characterizing the probability of droplet formation of the $k$-th size fraction of volume $x_k$ due to the breakup of a droplet of volume $v$. The first integral is zero for $i = 1$ while the second integral is zero for $i = k$.

To use (A.1), we specify the function $G$ suggested by Eskin et al. (2017b),

$$G(d) = K \frac{(\epsilon d)^{1/3}}{d} \left[ erfc(\Phi^{1/2}) + \frac{2}{\pi^{1/2}} \Phi^{1/2} \exp(-\Phi) \right], \tag{A.3}$$

where $erfc$ is the complimentary error function, $K$ is the model parameter, $\epsilon$ is the energy dissipation rate per unit mass, $\Phi = \dfrac{3}{2}\dfrac{We_{cr}}{We}$ is the dimensionless complex, $We = \dfrac{2\rho_f(\epsilon d)^{2/3}d}{\gamma}$ is the droplet Weber number, and $We_{cr}$ is the critical Weber number.

The critical Weber number determines the steady-state droplet size distribution. This number was identified from Couette device experimental data on dispersion of chemically stabilized water droplets in mineral oil as $We_{cr} = 0.5$ (Eskin et al., 2017b).

The parameter $K$ could not be determined accurately by the Couette device experiments because of extremely fast dispersion of chemically stabilized droplets in a turbulent flow (Eskin et al., 2017b). The time required for Couette device rotation start and stoppage was comparable to dispersion duration; thus, the evolution of droplet size distribution with time could not be measured. Cao et al. (2020), who studied $CO_2$ dispersion in turbulent water flow in a pipe, tuned the parameter $K$ to fit available experimental data.

In the present work, we employed the same breakup density function as Eskin et al. (2017a). This function is as follows (Lee et al., 1987):

$$\beta(f_{bv}) = 12 f_{bv}(1 - f_{bv}), \tag{A.4}$$

where $f_{bv} = v/x$ is the breakup fraction, and $x$ and $v$ are the mother and smaller droplet volumes respectively.

To use Eqs. (A.3) and (A.11), a distribution of the turbulent energy dissipation rate over the tubing radius needs to be calculated. The dissipation rate can be calculated as the specific power spent on friction between concentric fluid layers (Eskin et al., 2017a)

$$\epsilon(\tilde{r}) = \xi \frac{\tilde{r}^{3/2}}{1 - \tilde{r}}, \tag{A.5}$$

where $\tilde{r} = r/R$ is the dimensionless radius, $\xi = (-0.5\nabla p/\rho_f)^{1.5}\sqrt{R}/\kappa$ is a dimensional complex, $\kappa$ is the von Karman constant, and $\nabla p$ is the pressure gradient.

The pressure gradient $\nabla p$ is calculated as

$$\nabla p = -2\rho_f f U^2 / D. \tag{A.6}$$

In the present work, we assume a hydraulically smooth pipe. Thus, the Fanning friction factor $f$ can be calculated through the Blausius equation as (e.g. Bird et al., 2002)

$$f = \frac{0.079}{\text{Re}^{0.25}}, \tag{A.7}$$

where $\text{Re} = UD/\nu_f$ is the pipe Reynolds number.

## ii   Coalescence term

The rate of the droplet number concentration change due to coalescence is calculated as (Kumar and Ramkrishna, 1996)

$$\left(\frac{\partial N_i}{\partial t}\right)_{coal} = \sum_{\substack{j,k \\ x_{i-1} \leq x_j + x_k \leq x_{i+1}}}^{j \geq k} (1 - 0.5\delta_{jk})\eta Q_{j,k} N_j N_k - N_i \sum_{k=1}^{M} Q_{i,k} N_k, \tag{A.8}$$

where $\delta_{jk}$ is the Kronecker delta and $Q_{j,k}$ is the coalescence rate of droplets of sizes $j$ and $k$. The variable $\eta$ is calculated as

$$\eta = \begin{cases} \dfrac{x_{i+1} - v}{x_{i+1} - x_i}, & x_i \leq v \leq x_{i+1} \tag{A.9} \\[2mm] \dfrac{v - x_{i-1}}{x_i - x_{i-1}}, & x_{i-1} \leq v \leq x_i. \tag{A.10} \end{cases}$$

There are many different coalescence rate models available in the literature (e.g. Liao and Lucas, 2010). However, numerical analysis (Liao and Lucas, 2010) has demonstrated that different models predict significantly different results. In the current study, we employ a model suggested by Coulaloglou and Tavlarides (1977) that was employed by Cao et al.

25

(2020) for modeling $CO_2$ droplet dispersion in a pipe flow. According to this model, the coalescence rate is calculated as

$$Q_{j,k} = \alpha(d_j, d_k)\omega(d_j, d_k), \tag{A.11}$$

where $\alpha(d_j, d_k)$ is the coalescence efficiency, and $\omega(d_j, d_k)$ is the collision frequency of randomly fluctuating spheres. The collision frequency $\omega(d_j, d_k)$ can be calculated by a well-known equation (e.g. Coulaloglou and Tavlarides, 1977) as

$$\omega(d_j, d_k) = C_1(d_j + d_k)^2 \epsilon^{1/3} (d_j^{2/3} + d_k^{2/3})^{1/2}, \tag{A.12}$$

where $C_1$ is the model parameter.

The equation for the coalescence efficiency, suggested by Coulaloglou and Tavlarides (1977) is

$$\alpha(d_j, d_k) = \exp\left(-C_2 \frac{\mu_f \rho_f \epsilon}{\gamma^2} \left(\frac{d_j d_k}{d_j + d_k}\right)^4\right), \tag{A.13}$$

where $C_2$ is the model parameter.

The parameters $C_1$, $C_2$, identified under specific conditions can be found in the literature (e.g. Laakkonen et al., 2006). However, unique values of these parameters do not exist. In a prior study (Cao et al., 2020), $C_1 = 1$ was assumed. Note, this value is close to 0.88 as recommended by Laakkonen et al. (2006). The parameter $C_2$ was identified as $C_2 = 10^{13}$ to fit the experimental data (Zendehboudi et al., 2013).

### iii  Dissolution term

The dissolution term is calculated as follows (Cao et al., 2020):

$$\left(\frac{\partial N_i}{\partial t}\right)_{diss} = \frac{N_{i+1}}{x_{i+1} - x_i}\left|\frac{dx_{i+1}}{dt}\right|_{diss} - \frac{N_i}{x_i - x_{i-1}}\left|\frac{dx_i}{dt}\right|_{diss}, \tag{A.14}$$

where $(dx_i/dt)_{diss}$ is the rate of volume change of a droplet of the $i$-th size fraction only due to dissolution.

This equation was derived based on mass balance for a single droplet in the process of dissolution. Note that the dissolution of a single bubble/droplet in a turbulent flow is a well-studied phenomenon. For example, Lezhnin et al. (2003) published a comprehensive work on modeling the dissolution of an air bubble in a turbulent pipe water flow. The dissolution rate for the $i$-th size fraction droplet is calculated as

$$\left(\frac{dx_i}{dt}\right)_{diss} = -\frac{k\pi^{1/3}(6x_i)^{2/3}}{\rho_d}(C_s - C_\infty), \tag{A.15}$$

where $C_s$ is the saturation concentration of carbon dioxide in a bulk fluid, $C_\infty$ is the concentration of dissolved carbon dioxide in the fluid, $k = \dfrac{Sh D_{CO_2}}{d}$ is the droplet-fluid mass transfer coefficient, $Sh$ is the droplet Sherwood number, $D_{CO_2}$ is the molecular diffusivity of carbon dioxide in water and $\rho_d$ is the droplet density.

The Sherwood number for a droplet in a turbulent pipe flow can be calculated by the semi-empirical correlation as (Kress and Keyes, 1973)

$$Sh = 0.34\left(\frac{d_p}{D}\right)^2 Re^{0.94}Sc^{0.5}, \tag{A.16}$$

where $Sc = \nu_f/D$ is Schmidt number.

If no gas is initially dissolved in water, then the dissolved gas concentration evolution in-

creases as

$$C_\infty = \frac{\rho_d(\phi_0 - \phi)}{1 - \phi}, \tag{A.17}$$

where $\phi = \sum_{i=1}^{M} N_i x_i$ is the volume concentration of a dispersed phase, $\phi_0$ is the volume concentration of a dispersed phase at the initial time moment.

### iv  Solubility of carbon dioxide in water

The solubility calculation is reduced to determining the equilibrium concentration of carbon dioxide in water. The calculation method employed is based on the approach suggested by Spycher et al. (2003). The solubility of $CO_2$ in water-based brine can be determined from the molality $m_{CO_2}^0$ as $C_s = 0.04401 m_{CO_2}^0 \rho_d$. The molality is calculated as

$$m_{CO_2}^0 = \frac{55.508 x_{CO_2}}{1 - x_{CO_2}}, \tag{A.18}$$

where $x_{CO_2}$ is the $CO_2$ mole fraction in the aqueous phase, calculated as

$$x_{CO_2} = B(1 - y_{H_2O}), \tag{A.19}$$

and $y_{H_2O}$ is the mole fraction of water in the vapor phase,

$$y_{H_2O} = \frac{1 - B}{1/A - B}. \tag{A.20}$$

The parameters $A$ and $B$ are calculated as

$$B = \frac{\phi_{CO_2} p}{55.508 k_{CO_2(g)}^0} \exp\left[-\frac{(p - p^0)\bar{V}_{CO_2}}{RT}\right] \tag{A.21}$$

$$A = \frac{k_{H_2O(g)}^0}{\phi_{H_2O} p} \exp\left[\frac{(p - p^0)\bar{V}_{H_2O}}{RT}\right], \tag{A.22}$$

28

where $\bar{V}_{H_2O} = 18.1$ cm³/mol, $\bar{V}_{CO_2}(g) = 32.6$ cm³/mol and $\bar{V}_{CO_2}(l) = 32$ cm³/mol, $p$ is the local pressure, $p_0$ is the initial pressure, $R$ is the gas constant, $T$ is the temperature. The $k$ parameters for $CO_2$ and water are

$$k^0_{CO2(g)} = \exp(1.189 + 1.304 \times 10^{-2}T - 5.446 \times 10^{-5}T^2) \tag{A.23}$$

$$k^0_{CO2(l)} = \exp(1.169 + 1.368 \times 10^{-2} - 5.380 \times 10^{-5}T^2) \tag{A.24}$$

$$k^0_{H_2O} = \exp(-2.209 + 3.097 \times 10^{-2}T - 1.098 \times 10^{-4}T^2 + 2.048 \times 10^{-7}T^3), \tag{A.25}$$

where $T$ is in °C. The fugacity coefficients, $\phi_{CO_2}$, $\phi_{H_2O}$ can be determined as

$$\ln(\phi_k) = \ln\left(\frac{V}{V - b_m}\right) + \left(\frac{b_k}{V - b_m}\right) - \left(\frac{2\sum_{i=1}^{n} y_i a_{ik}}{RT^{1.5}b_m}\right)\ln\left(1 + \frac{b_m}{V}\right)$$
$$+ \left(\frac{a_m b_k}{RT^{1.5}b_m^2}\right)\left[\ln\left(1 + \frac{b}{V}\right) - \left(\frac{b_m}{V + b_m}\right)\right] - \ln\left(\frac{PV}{RT}\right). \tag{A.26}$$

The volume of the dispersed phase is determined by solving the cubic equation:

$$V^3 - V^2\left(\frac{RT}{p}\right) - V\left(\frac{RTb}{p} - \frac{a}{pT^{0.5}} + b^2\right) - \left(\frac{ab}{pT^{0.5}}\right) = 0, \tag{A.27}$$

where $p$ is determined through the Redlich-Kwong equation of state (Redlich and Kwong, 1949)

$$p = \frac{RT}{V - b} - \frac{a}{T^{0.5}V(V + b)}. \tag{A.28}$$

The parameters $a, b$, calculated using mixing rules (Prausnitz et al., 1986) are

$$a_m = y_{H_2O}^2 a_{H_2O} + 2y_{H_2O}y_{CO_2}a_{H_2O-CO_2} + y_{CO_2}^2 a_{CO_2} \tag{A.29}$$

$$b_m = y_{H_2O}b_{H_2O} + y_{CO_2}b_{CO_2}, \tag{A.30}$$

where the parameters $a_{\text{CO}_2}, b_{\text{CO}_2}, b_{\text{H}_2\text{O}}, a_{\text{H}_2\text{O}-\text{CO}_2}$ are reported in Spycher et al. (2003) as

$$a_{\text{CO}_2} = 7.54 \times 10^{-7} - 4.13 \times 10^4 \times T(K) \text{ bar cm}^6 \text{ K}^{0.5} \text{ mol}^{-2} \qquad \text{(A.31)}$$

$$b_{\text{CO}_2} = 27.80 \text{ cm}^3/\text{mol} \qquad \text{(A.32)}$$

$$b_{\text{H}_2\text{O}} = 18.18 \text{ cm}^3/\text{mol} \qquad \text{(A.33)}$$

$$a_{\text{H}_2\text{O}-\text{CO}_2} = 7.89 \times 10^7 \text{ bar cm}^6 \text{ K}^{0.5} \text{ mol}^{-2}, \qquad \text{(A.34)}$$

where $T$ is in the range $283 - 380$ K.

# Acknowledgement

# References

(1) *World Energy Outlook 2019*; IEA: Paris, 2019.

(2) Boden, T. A.; Marland, G.; Andres, R. J. *Global, Regional, and National Fossil-Fuel $CO_2$ Emissions*; Carbon Dioxide Information Analysis Center, Oak Ridge National Laboratory, U.S. Department of Energy: Oak Ridge, Tenn., U.S.A., 2017.

(3) Metz, B.; Davidson, O.; de Coninck, H.; Loos, M.; Meyer, L. *Carbon Dioxide Capture and Storage: Special Report of the Intergovernmental Panel on Climate Change*; Cambridge University Press: New York, 2005.

(4) Herzog, H. J. What future for carbon capture and sequestration? *Environ. Sci. Technol.* **2001**, *35 (7)*, 148A–153A.

(5) Jenkins, C. R. et al. Safe storage and effective monitoring of $CO_2$ in depleted gas fields. *Proc. Natl. Acad. Sci. U.S.A.* **2012**, *109 (2)*, E35–E41.

(6) Shi, J.-Q.; Durucan, S. $CO_2$ Storage in Deep Unminable Coal Seams. *Oil & Gas Science and Technology – Rev. IFP* **2005**, *60 (3)*, 547–558.

(7) Celia, M. A.; Bachu, S.; Nordbotten, J. M.; Bandilla, K. W. Status of $CO_2$ storage in deep saline aquifers with emphasis on modeling approaches and practical simulations. *Water Resour. Res.* **2015**, *51*, 6846–6892.

(8) Haugan, P. M.; Joos, F. Metrics to assess the mitigation of global warming by carbon capture and storage in the ocean and in geological reservoirs. *Geophys. Res. Lett.* **2004**, *31*, L18202.

(9) International Energy Agency (IEA), *$CO_2$ Capture and Storage*; IEA Publications, 2008.

(10) Benson, S. M.; Cole, D. R. *$CO_2$ Sequestration in Deep Sedimentary Formations. Elements* **2008**, *4(5)*, 325–331.

(11) Ghaderi, S. M.; Leonenko, Y. *Reservoir Modeling for Wabamun Area $CO_2$ Sequestration Project (WASP)*; Energy and Environmental Systems Group, Institute for Sustainable Energy, Environment and Economy (ISEEE): Waterloo, Canada, 2009.

(12) Ghaderi, S. M.; Leonenko, Y. Reservoir modeling for Wabamun lake sequestration project. *Energy Science & Engineering* **2015**, *3(2)*, 98–114.

(13) van der Meer, L. G. H. The Conditions Limiting $CO_2$ Storage in aquifers. *Energy Convers. Manage.* **1993**, *34*, 959–966.

(14) Lindeberg, E. Escape of $CO_2$ from aquifers. *Energy Convers. Manage.* **1997**, *38*, S235–S240.

(15) Emami-Meybodi, H.; Hassanzadeh, H.; Green, C. P.; Ennis-King, J. Convective dissolution of $CO_2$ in saline aquifers: Progress in modeling and experiments. *Int. J. Greenh. Gas Con.* **2015**, *40*, 238–266.

(16) Hassanzadeh, H.; Pooladi-Darvish, M.; Keith, D. W. Accelerating $CO_2$ dissolution in saline aquifers for geological storage - Mechanistic and sensitivity studies. *Energy & Fuels* **2009**, *23(6)*, 3328–3336.

(17) Keith, D. W.; Hassanzadeh, H.; Pooladi-Darvish, M. *Greenhouse Gas Control Technologies*, 7th ed.; Elsevier Science Ltd: Oxford, 2005; pp 2163–2167.

(18) Leonenko, Y.; Keith, D. W. Reservoir engineering to accelerate the dissolution of $CO_2$ stored in aquifers. *Environ. Sci. Technol.* **2008**, *42(8)*, 2742–2747.

(19) Zirrahi, M.; Hassanzadeh, H.; Abedi, J. Modeling of $CO_2$ dissolution by static mixers using back flow mixing approach with application to geological storage. *Chem. Eng. Sci.* **2013a**, *104*, 10–16.

(20) Zirrahi, M.; Hassanzadeh, H.; Abedi, J. The laboratory testing and scale-up of a down-hole device for $CO_2$ dissolution acceleration. *Int. J. Greenh. Gas Con.* **2013b**, *16*, 41–49.

(21) Shafaei, M. J.; Abedi, J.; Hassanzadeh, H.; Chen, Z. Reverse gas-lift technology for $CO_2$ storage into deep saline aquifers. *Energy* **2012**, *45(1)*, 840–849.

(22) Zendehboudi, S.; Khan, A.; Carlisle, S.; Leonenko, Y. *Ex Situ* Dissolution of $CO_2$: A New Engineering Methodology Based on Mass-Transfer Perspective for Enhancement of $CO_2$ Sequestration. *Energy & Fuels* **2011**, *25*, 3323–3333.

(23) Cholewinski, A.; Leonenko, Y. Ex-situ Dissolution of $CO_2$ for Carbon Sequestration. *Energy Procedia* **2013**, *37*, 5427–5434.

(24) Leonenko, Y. *Cutting-Edge Technology for Carbon Capture, Utilization, and Storage*; John Wiley & Sons, Ltd, 2018; Chapter 4, pp 47–58.

(25) Cao, F.; Eskin, D.; Leonenko, Y. Modeling of Ex-Situ Dissolution for Geologic Sequestration of Carbon Dioxide in Aquifers. *J. Petrol. Sci. Eng.* **2020**, *187*, 106835.

(26) Eskin, D.; Taylor, S.; Ma, S. M.; Abdallah, W. Modeling droplet dispersion in a vertical turbulent tubing flow. *Chem. Eng. Sci.* **2017a**, *173*, 12–20.

(27) Schlichting, H.; Gersten, K. *Boundary-Layer Theory*; Springer, Berlin, 2000.

(28) Johansen, S. T. The deposition of particles on vertical walls. *Int. J. Multiph. Flow* **1991**, *17*, 355–376.

(29) DiPietro, J. A. *Landscape Evolution in the United States : An Introduction to the Geography, Geology, and Natural History*; Elsevier Science Publishing Co Inc: United States, 2013.

(30) Bahonar, M.; Azaiez, J.; Chen, Z. Two Issues in Wellbore Heat Flow Modelling Along With the Prediction of Casing Temperature in the Steam Injection Wells. *J. Can. Petrol. Technol.* **2011**, *50 (1)*, 43–63.

(31) Incropera, F. P.; DeWitt, D. P. *Fundamentals of Heat and Mass Transfer*; John Wiley & Sons, Inc.: New York City, New York, 1996.

(32) Coker, A. K. *Fortran Programs for Chemical Process Design, Analysis, and Simulation*; Gulf Professional Publishing, 1995; pp 103–149.

(33) Fontanilla, J.; Aziz, K. Prediction of Bottom-Hole Conditions for Wet Steam Injection Wells. *J. Can. Pet. Technol.* **1982**, *21(2)*, 82–88.

(34) Ramey, H. J. Wellbore Heat Transmission. *J. Pet. Technol.* **1962**, *14(4)*, 427–435.

(35) Hasan, A.; Kabir, C. Aspects of wellbore heat transfer during two-phase flow. *SPE Production and Facilities (Society of Petroleum Engineers); (United States)* **1994**, *9:3*.

(36) Levich, V. G. *Physicochemical Hydrodynamics*; Prentice-Hall, Englewood Cliffs, NJ, 1962.

(37) Likhachev, E. Dependence of water viscosity on temperature and pressure. *Tech. Phys.* **2003**, *48*, 514–515.

(38) Bachu, S.; Bennion, B. Dependence of $CO_2$-brine interfacial tension on aquifer pressure, temperature and water salinity. *Energy Procedia* **2009**, *1(1)*, 3157–3164.

(39) Nielsen, L. C.; Bourg, I. C.; Sposito, G. Predicting $CO_2$–water interfacial tension under pressure and temperature conditions of geologic CO2 storage. *Geochimica et Cosmochimica Acta* **2012**, *81*, 28–38.

(40) Spycher, N.; Pruess, K.; Ennis-King, J. $CO_2 - H_2O$ mixtures in the geological sequestration of $CO_2$. I. Assessment and calculation of mutual solubilities from 12 to 100 °C and up to 600 bar. *Geochimica et Cosmochimica Acta* **2003**, *67 (16)*, 3015–3031.

(41) Hassanzadeh, H.; Pooladi-Darvish, M.; Elsharkawy, A.; Keith, D.; Leonenko, Y. Predicting PVT data for $CO_2$–brine mixtures for black-oil simulation of $CO_2$ geological storage. *Int. J. Greenh. Gas. Con.* **2008**, *2*, 65–77.

(42) Kumar, S.; Ramkrishna, D. On the solution of population balance equations by discretization-I. A fixed pivot technique. *Chem. Eng. Sci.* **1996**, *51*, 1311–1332.

(43) Eskin, D.; Taylor, S.; Dingzheng, Y. Modeling of droplet dispersion in a turbulent Taylor-Couette flow. *Chem. Eng. Sci.* **2017b**, *161*, 36–47.

(44) Lee, C.; Glasgow, L.; Erickson, L. Bubble breakup and coalescence in turbulent gas–liquid dispersions. *Chem. Eng. Commun.* **1987**, *59*, 65–84.

(45) Bird, B. R.; Stuart, W. E.; Lightfoot, E. N. *Transport Phenomena*; John Wiley & Sons Inc, New York/Toronto, 2002.

(46) Liao, Y.; Lucas, D. A literature review on mechanisms and models for the coalescence process of fluid particles. *Chem. Eng. Sci.* **2010**, *65*, 2851–2864.

(47) Coulaloglou, C.; Tavlarides, L. Description of interaction processes in agitated liquid–liquid dispersions. *Chem. Eng. Sci.* **1977**, *32*, 1289–1297.

(48) Laakkonen, M.; Alopaeus, V.; Aittamaa, J. Validation of bubble breakage, coalescence and mass transfer models for gas–liquid dispersion in agitated vessel. *Chem. Eng. Sci.* **2006**, *61*, 218–228.

(49) Zendehboudi, S.; Shafiei, A.; Bahadori, A.; Leonenko, Y.; Chatzis, I. Droplets evolution during ex situ dissolution technique for geological $CO_2$ sequestration: Experimental and mathematical modelling. *Int. J. Greenh. Gas Con.* **2013**, *13*, 201–214.

(50) Lezhnin, S.; Eskin, D.; Leonenko, Y.; Vinogradov, O. Dissolution of air bubbles in a turbulent water pipeline flow. *Heat and Mass Transfer* **2003**, *39*, 483–487.

(51) Kress, T. S.; Keyes, J. J. Liquid phase controlled mass transfer to bubbles in cocurrent turbulent pipeline flow. *Chem. Eng. Sci.* **1973**, *28*, 1809–1823.

(52) Redlich, O.; Kwong, J. On the Thermodynamics of Solutions. V. An Equation of State. Fugacities of Gaseous Solutions. *Chem. Rev.* **1949**, *44*, 233–244.

(53) Prausnitz, J.; Lichtenthaler, R. N.; de Azevedo, E. G. *Molecular Thermodynamics of Fluid-Phase equilibria*; Prentice Hall: New Jersey, 1986.